



# Computer graphics simulation of natural mummification by desiccation

Dhana Frerichs<sup>1</sup> | Andrew Vidler<sup>1</sup> | Christos Gatzidis<sup>2</sup>

<sup>1</sup>R&D Department, Ninja Theory Ltd., Cambridge, UK

<sup>2</sup>Department Creative Technology, Faculty of Science and Technology, Bournemouth University, Poole, UK

## Correspondence

Dhana Frerichs, Ninja Theory Ltd., Cambridge, UK.  
Email: dhana.frerichs@ninjatheory.com

## Abstract

Organic bodies are subject to internal processes after death, causing significant structural, and optical changes. Mummification by desiccation leads to volume shrinkage, skin wrinkling, and discoloration. We propose a method to simulate the process of mummification by desiccation and its effects on the corpse's morphology and appearance. The mummifying body is represented by a layered model consisting of a tetrahedral mesh, representing the volume, plus a high resolution triangle surface mesh representing the skin. The finite element method is used to solve the moisture diffusion and the resulting volume deformations. Skin wrinkling is achieved using position based dynamics. In order to model a visually believable reproduction of the skin coloration changes due to mummification, a skin shading approach is used that considers moisture content, hemoglobin content, and oxygen saturation. The main focus of the work in this article is to recreate the appearance changes of mummification by desiccation, which, to the best of our knowledge, has not been attempted before in computer graphics to this level of realism. The suggested approach is able to model changes in the internal structure and the surface appearance of the body which resemble the postmortem processes of natural mummification by desiccation.

## KEYWORDS

appearance modeling, decomposition, mummification, physical-based simulation

## 1 | INTRODUCTION

Human body decomposition is a complex degenerative process, comprising of a number of biological, chemical, and physical activities. The occurrence of these activities depends greatly on the object's environment. Some can happen concomitantly while others are mutually exclusive. There is no single combination of processes that drive the decomposition and, as such, the appearance of corpses varies greatly. Although object weathering and decomposition has received more attention in recent years, the realistic depiction of human and other organic corpses has been neglected. We focus on one aspect of human body decomposition, namely, natural mummification by desiccation, with the aim to develop methods to recreate postmortem appearance changes due to soft tissue dehydration that are comparable to their real world equivalents.

Mummification by desiccation is caused by water evaporation in dry environments. This leads to the shrinking of the body and the wrinkling of the skin. A physically based approach is used to simulate the processes and appearance changes associated with natural mummification by desiccation. The simulation consists of four parts; humidity diffusion, volume

This is an open access article under the terms of the Creative Commons Attribution License, which permits use, distribution and reproduction in any medium, provided the original work is properly cited.

© 2020 The Authors. *Computer Animation and Virtual Worlds* published by John Wiley & Sons, Ltd.

deformation, skin deformation and, finally, skin shading. The finite element method (FEM)<sup>1</sup> is employed to simulate the moisture diffusion and the resulting deformation. Position based dynamics<sup>2</sup> are used in order to achieve the associated skin shriveling and wrinkling effects. The changes in skin coloration are achieved by employing a layered skin shader approach that is capable of producing believable coloration changes to the skin, caused by changes in hemoglobin, oxygen saturation, and moisture.

The mummification method is applied to models of a human arm and head with internal flesh and bone layers and an outer skin layer. Images are generated of the resulting postmortem appearance. These will be compared with photographs of dead bodies that have been subject to the analogous real world decay processes plus descriptions of these processes in literature. The humidity diffusion is evaluated by examining whether its progression follows the same patterns expected from the description in dehydration literature. Visual comparison of the simulation results with photographs of desiccated mummies is used to evaluate the realism of the volume shrinking, skin deformation, and skin shading. In addition, the progression of the simulated mummification is compared with descriptions and photographs at different stages of an experimental mummification of a human lower leg.

## 2 | RELATED WORK

There has been an increasing trend toward computer generation of object weathering, ageing, and decomposition effects as shown by Frerichs et al.<sup>3</sup> and Gibson and Mirtich.<sup>4</sup> Considerable work has been carried out in creating ageing and weathering effects that mainly affect the surface appearance, such as cracks and fractures,<sup>5,6</sup> corrosion,<sup>7</sup> rusting,<sup>8</sup> patinas,<sup>9</sup> staining,<sup>10</sup> and general surface weathering approaches.<sup>11,12</sup> These involve adding or removing material from the object's surface.

Organic decomposition has received less attention. As opposed to the processes mentioned above, organic decomposition generally involves a deformation of the object, rather than loss of material from its surface. Examples of organic decomposition in computer graphics include leaf withering,<sup>13</sup> fruit rotting,<sup>13,14</sup> and livor mortis.<sup>15</sup> Leaf withering is achieved by simulating the osmotic water flow in the leaf's veins.<sup>13</sup> A layered model consisting of a triangle mesh and a Voronoi diagram represents the leaf, where the edges represent the leaf's veins and act as springs. The vertices hold information on water and solute concentration. Changes in water content cause leaf deformation and discoloration. However, Jeong et al.<sup>13</sup> only consider thin shell objects and their method cannot be easily translated to volumetric objects, such as fruit or animal carcasses. Work on other organic thin shell objects, such as skin ageing and wrinkling on living humans, has also been addressed.<sup>16,17</sup>

Kider et al.<sup>18</sup> and Lui et al.<sup>14</sup> worked on simulating fruit rotting. Fruits, like animal bodies, are made of different materials which respond to decomposition in different manners. Kider et al.<sup>18</sup> and Lui et al.<sup>14</sup> propose a method for fruit rotting that uses a layered representation for the fruit skin and flesh. The fruit skin is represented by a surface mesh and the internal volume, which represents the fruit flesh and kernel, by mass points. Volume shrinkage and skin wrinkling is achieved by treating the triangle mesh and volume as mass-spring systems. Texture maps that hold nutrient and soft rot information on the object's surface can be used for a reaction diffuse lighting model in order to guide fungal growths. Lui et al.<sup>14</sup> use a similar layered representation for fruit rotting, but employ a tetrahedral mesh to represent the fruit flesh and kernel.

Tetrahedral meshes have proven successful in modeling human tissue for interactive tissue surgery simulators.<sup>19-22</sup> They allow the definition of the interior of a volume, which is not possible with surface meshes. Furthermore, they can act as finite element discretization for physically based simulation based on continuum mechanics, as shown by Lui et al.,<sup>14</sup> who use a FEM to solve the moisture diffusion equation within the fruit in order to simulate dehydration and the subsequent volume deformation. The skin and volume layers are connected by springs that pull the skin along as the volume mesh deforms. Frerichs et al.<sup>15</sup> use a similar model to represent a volumetric model for simulating livor mortis. The skin discolorations called livor mortis are achieved by modeling the blood dynamics in the body after death. The blood dynamics are simulated by moving blood between tetrahedral vertices along connecting edges. As opposed to Jeong et al.<sup>13</sup> and Kider et al.,<sup>18</sup> the blood dynamics are controlled by gravity. Their method only handles skin coloration caused by the blood dynamics inside the body, so no volume deformation is modeled.

## 3 | BIOLOGICAL BACKGROUND ON NATURAL MUMMIFICATION

Aufderheide<sup>23</sup> describes a mummy as a corpse or tissue that has been preserved to such a degree that it resembles its living morphology and resists further decay. Mummification can happen naturally in certain environmental conditions

(natural mummification) or by human intervention (artificial mummification), like Egyptian mummies. Natural mummification can occur for a variety of reasons. A well-known example is mummification by desiccation in hot, dry, and arid environments. Others include (but are not restricted to) freezing, bog bodies, or due to exposure to certain metals. For this article, only natural mummification by desiccation is considered. For more information on general mummification see Aufderheide<sup>23</sup> and Lynnerup.<sup>24</sup>

In order to simulate this process an understanding of the visual and morphological changes as well as the processes that drive them needs to be outlined. For mummification by desiccation the evaporation and diffusion of water in the body are important. About 80% of human tissue is removable water.<sup>23</sup> The degree of desiccation often varies over the body, depending on the volume to surface area ratio. The quickest desiccating parts are often also the ones with the best-preserved soft tissue in natural mummified bodies, such as fingers, toes, and ear lobes. An object that consists of a high percentage of water undergoes noticeable morphological changes with water loss. The gradual removal of the water leads to shrinking and shriveling of soft tissue and internal organs. The skin becomes dry and leathery, takes on a blackish-brown color and clings firmly to the body frame. Naturally desiccated tissue varies from black-brown to parchment cultured. During dehydration, the connection between the skin layers weakens, which leads to the epidermis separating from the dermis (skin slippage) and the dermis separating from the underlying tissue.

Papageorgopoulou et al.<sup>25</sup> describe research on modeling ancient Egyptian mummification on a “fresh” human lower leg. They identified humidity, external temperature and PH values as important factors in mummification. Papageorgopoulou et al. noticed that the leg undergoes drastic coloration changes, starting with a greenish discoloration in some areas which then spreads over the whole leg. The leg then started to turn dark green, grayish and brown and, finally, yellowish with patches of dark green, brown, and red. The foot shrunk at a faster rate than the rest of the leg. They noticed a significant loss of volume and a weight loss of 30% during the first two months and 50% by the end of the experiment, caused by water loss.

## 4 | OBJECT REPRESENTATION

The human body is a heterogeneous mass where each component responds differently to the decay process. In the case of mummification, the flesh parts (i.e., muscle and fat layers) shrink considerably, whereas the bones do not deform at all. The body's skin also undergoes some structural changes, such as shrinking and wrinkling. For the purpose of this article, the body is considered to be made of bones, flesh, and skin, though a more complicated body with organs is also possible to mummify with this model. Similarly to previous methods on fruit rotting<sup>14</sup> and livor mortis,<sup>15</sup> the skin is represented by a triangle surface mesh and the internal components, such as flesh and bones, are represented by a surface aligned tetrahedral mesh. The two layers are connected by tracking constraints, as in the livor mortis process.<sup>15</sup> The results will be rendered on a surface mesh, therefore, a mesh-based approach is used for the object representation during simulation.

Moisture content information is assigned to the tetrahedral vertices. Flesh and bone materials are differentiated by the moisture content assigned to their vertices. Bone vertices hold no moisture, whereas flesh nodes hold a percentage of moisture saturation. The tetrahedral meshes used in this article were constructed using a free tetrahedralization tool.<sup>26</sup> A high detail triangle mesh is chosen as the representation of the body's outer layer, which, for the purpose of the mummification simulation, represents the outer skin layer (epidermis). Using triangle meshes has many advantages, particularly in real-time applications, as they are faster to render and support the use of texture maps. The tracking constraints connect each node of the triangle mesh to a point on the boundary of the tetrahedral mesh and drive the deformation of the skin as the underlying volume mesh shrinks.

## 5 | BACKGROUND ON THE FEM

The FEM is a numerical technique for solving boundary value problems for a specific field variable  $\mathbf{u}$ , such as moisture (scalar) or position (vector).<sup>1</sup> The following shows a differential equation with field variable  $\mathbf{u}$ :

$$-\Delta \mathbf{u} + \rho \mathbf{u} = \mathbf{f}, \quad (1)$$

where the unknown  $\mathbf{u}$  can be a scalar valued (moisture) or vector valued (position) function,  $\rho$  is a nonnegative constant (usually density),  $-\Delta \mathbf{u}$  is the diffusion term and  $f$  describes the forces acting on the object. A finite element discretization

is used to express the infinite number of points within the object by a finite number of values. In this case, the object is divided into tetrahedral elements with finite volume. Every point within the polygonal element can then be expressed by an analytical function, called the shape or interpolation function, shown in Equation (2) below.

$$N_i(x, y, z) = a_i + b_i x + c_i y + d_i z. \quad (2)$$

Using the shape function, the field variable  $\mathbf{u}$  can be interpolated at any point within a tetrahedral element  $e$  as follows:

$$\mathbf{u} = \sum_{i=1}^n \mathbf{u}_i \mathbf{N}_i^e, \quad (3)$$

where  $\mathbf{u}_i$  is the value of the field variable at the tetrahedral vertex  $i$  and  $\mathbf{N}_i^e$  is the matrix representation of the shape function.

With this, Equation (1) can be rewritten into its weak form using Green's theorem:<sup>1</sup>

$$\int_V \nabla \mathbf{u} \cdot \nabla \mathbf{N} \, dV + \rho \int_V \mathbf{u} \mathbf{N} \, dV = \int_V f \mathbf{N} \, dV + \int_A (\partial_n \mathbf{u}) \mathbf{N} \, dA. \quad (4)$$

The weak formulation is used to solve the differential equation for  $\mathbf{u}$  on the vertices of the finite element discretization.

## 6 | HUMIDITY DIFFUSION

We are modifying the methods used by Liu et al.<sup>14</sup> and Yang et al.<sup>27</sup> to apply them to the problem of mummification by desiccation. The deformations observed in mummification by desiccation are driven by the changes in the tissue moisture content. As such, the first part of the mummification simulation is a simulation of the moisture evaporation from the object's surface and diffusion within the object. The drying process has been simulated on a slice of a potato using the FEM by Yang et al.<sup>27</sup> Liu et al.<sup>14</sup> use a similar method to simulate fruit rotting.

### 6.1 | Mathematical background on humidity diffusion

The humidity differences in the air and object cause vapor pressure differences in the air and boundary of the object. This leads to moisture exchange between the air and the object's surface. If the humidity in the air surrounding the object is lower than the humidity in the object itself, water leaves the object due to evaporation. Inside the object the water moves to the more dehydrated areas.

Yang et al.<sup>27</sup> and Liu et al.<sup>14</sup> express the moisture diffusion with the following boundary value problem: Let  $\phi(x, y, z, t)$  be the moisture content at any point  $(x, y, z)$  at a time  $t$ . Then, the moisture diffusion inside the object can be expressed as the following

Find  $\phi$  such that

$$\rho \frac{\partial \phi}{\partial t} = \nabla \cdot (w \rho \nabla \phi) \quad \text{moisture diffusion,} \quad (5)$$

$$\nabla \phi \cdot \mathbf{n} = \frac{h_m (\phi_e - \phi)}{w \rho} \quad \text{boundary condition,} \quad (6)$$

where  $\rho$  is the density of the solid,  $w$  is the moisture diffusion coefficient,  $\phi_e$  is the equilibrium moisture content in the surrounding air,  $h_m$  is the mass transfer coefficient, and  $\mathbf{n}$  is the normal of the boundary surface.  $\rho$  and  $w$  are functions of time that need to be recalculated at each time step. Yang et al.<sup>27</sup> and Liu et al.<sup>14</sup> provide the following formulas for this:

$$\rho(t) = \frac{\rho_0}{S_V}, \quad (7)$$

$$w(t) = w_0 \exp\left(-\frac{\phi_0}{\phi}\right), \quad (8)$$

where  $w_0$ ,  $\phi_0$ , and  $\rho_0$  are the initial moisture content, the solid density, and the initial density, respectively.  $S_V = \mu \frac{\phi}{\phi_0} + \lambda$  is the volumetric moisture shrinking coefficient that describes how much the element shrinks based on its moisture loss. The volume shrinkage coefficient that we used here will be described in more detail in the Humidity Interface section.

## 6.2 | FEM formulation of the humidity diffusion equation

We use the FEM to solve the moisture diffusion problem, similar to Liu et al.<sup>14</sup> We reconstruct the formula using Green's theorem<sup>1</sup> instead of using the one provided by Liu et al.

The moisture content  $\phi$  is defined at each vertex of the tetrahedralization. Let  $\Omega$  be the set of tetrahedral volume elements and  $\Gamma$  be the set of tetrahedral boundary elements. Making use of Green's theorem, as stated by Reddy and Gartling,<sup>1</sup> the Boundary Value Problem from Equation (5) can be rewritten as follows:

$$\int_{\Omega^e} \nabla \phi \nabla \mathbf{N}_i^e dV + \int_{\Omega^e} \rho \frac{\partial \phi}{\partial t} \mathbf{N}_i^e dV + \int_{\Gamma^e} h_m \phi \mathbf{N}_i^e dA = \int_{\Gamma^e} h_m \phi_e \mathbf{N}_i^e dA, \quad (9)$$

for all vertices  $i$ . Using Equations (3) and (4) the above becomes

$$\sum_{j \in \text{vertices}} \left( \mathbf{M}_{ij} \frac{\partial \phi_j}{\partial t} + (\mathbf{K}_{ij} + \mathbf{H}_{ij}) \phi_j \right) = \mathbf{f}_i, \quad (10)$$

where

$$\mathbf{K}_{ij}^e = \int_{\Omega^e} \nabla \mathbf{N}_j^e \cdot \nabla \mathbf{N}_i^e dV, \quad (11)$$

$$\mathbf{M}_{ij}^e = \int_{\Omega^e} \rho \mathbf{N}_j^e \cdot \mathbf{N}_i^e dV, \quad (12)$$

$$\mathbf{H}_{ij}^e = \int_{\Gamma^e} h_m \mathbf{N}_j^e \cdot \mathbf{N}_i^e dA, \quad (13)$$

$$\mathbf{f}_i^e = \int_{\Gamma^e} h_m \phi_e \mathbf{N}_i^e dA, \quad (14)$$

for each tetrahedral element  $e$ . This is our reconstruction of the equation used by Liu et al.<sup>14</sup> The integrals in Equations (11) to (14) can be solved and assembled into their global matrices and global vector ( $\mathbf{K}$ ,  $\mathbf{M}$ ,  $\mathbf{H}$ , and  $\mathbf{f}$ ) using the Eisenberg and Malvern approach.<sup>28</sup> After the matrix assembly, the time-dependent linear equation for the whole object can be expressed as the following linear equation:

$$\mathbf{M} \frac{\partial \phi}{\partial t} + (\mathbf{K} + \mathbf{H}) \phi = \mathbf{f}, \quad (15)$$

at time  $t$ . In order to compute  $\phi$  at any time, the equation needs to be integrated over time. The time from  $t_0$  can be partitioned into time intervals, such that time step is  $\Delta t = t_{n+1} - t_n$ . Applying this to Equation (15) and rearranging it with respect to  $\phi^{n+1}$  yields the following linear equation:

$$(\mathbf{M} + \Delta t(\mathbf{K} + \mathbf{H})) \phi^{t+1} = \mathbf{M} \phi^t + \Delta t \mathbf{f}^{t+1}. \quad (16)$$

Now the linear equation can be solved for the unknown  $\phi$  at each time step (using any algorithm for solving linear equations).

## 7 | VOLUME DEFORMATION

Water loss causes the tissue to shrink, resulting in a visible loss of volume. The soft tissue, such as skin and flesh, gets compressed whereas bones do not change. For the mummification method a differential equation is constructed from Newton's second law of motion that describes the dynamic deformation of an object based on Hooke's law.<sup>29</sup> This is then formulated in a FEM framework, as with the humidity diffusion in the previous section.

### 7.1 | Physical background on deformation

This section gives a very short overview of physical deformations, summarizing Nealen et al.,<sup>29</sup> Liu et al.,<sup>14</sup> and Müller and Gross.<sup>30</sup> The deformation of a continuous object can be described by continuum mechanics in terms of forces ( $\mathbf{f}$ ), stresses ( $\sigma$ ), and strains ( $\epsilon$ ). Deformation of an object occurs when a force is applied to its surface which, in turn, exerts strain on the affected material. Strain is the relative expansion or compression of a material due to stress. This is expressed by Hooke's law for continuous media:<sup>29</sup>

$$\sigma = \mathbf{E}\epsilon, \quad (17)$$

where  $\mathbf{E}$  is the stiffness matrix.<sup>14</sup>

For the deformation simulation, the object is considered to be a continuous three-dimensional elastic solid. Both the stress and strain tensor have six distinct values and are expressed by the six-dimensional vectors  $\sigma$  and  $\epsilon$ , respectively.

For this article, the Cauchy linear strain tensor<sup>29</sup> is used to compute the strain tensor which looks as follows:

$$\epsilon = \frac{1}{2}(\nabla \mathbf{u} + [\nabla \mathbf{u}]^T), \quad (18)$$

where  $\mathbf{u}$  is the displacement. Newton's second law of motion for an object with constant mass states that  $\mathbf{f} = m\mathbf{a}$ , where  $m$  is the object's mass. This can be described in terms of external and internal body forces acting on the element at point  $\mathbf{x} \in \mathbb{R}^3$ :

$$\rho \ddot{\mathbf{x}} = \mathbf{f}(\mathbf{x})_{\text{ext}} + \mathbf{f}(\mathbf{x})_{\text{int}}. \quad (19)$$

The internal forces  $\mathbf{f}_{\text{int}}(\mathbf{x})$  acting on  $\mathbf{x}$  are due to internal stress and, using Equation (17), can be expressed by:

$$\mathbf{f}_{\text{int}} = \nabla(\mathbf{E}\epsilon). \quad (20)$$

This yields the following equation in terms of strain:

$$\rho \ddot{\mathbf{x}} = \nabla(\mathbf{E}\epsilon) + \mathbf{f}_{\text{ext}} \quad (21)$$

This equation can be used to compute the changes in positions  $\dot{\mathbf{x}}$  using the FEM.

### 7.2 | FEM formulation of the deformation

Following the approach by Liu et al.<sup>14</sup> and Yang et al.,<sup>27</sup> we use the FEM to solve the deformation of the volume mesh. The deformation of an object is described by a vector field  $\mathbf{u}(\mathbf{x})$  for every point  $\mathbf{x}$  in the continuous object. In order to model the deformation, the displacement  $\mathbf{u}$  for any point in the object needs to be determined in order for the new positions  $\mathbf{x}$  to be computed. This can be achieved with the help of the FEM in a similar manner to the humidity diffusion.

Let  $\mathbf{B} = \Delta\mathbf{N}$ , then strain can be expressed as  $\boldsymbol{\varepsilon} = \mathbf{B}\mathbf{u}$  and stress becomes  $\boldsymbol{\sigma} = \mathbf{E}\boldsymbol{\varepsilon} = \mathbf{E}\mathbf{B}\mathbf{u}$ . Then, Equation (19) can be rewritten in terms of the tetrahedral vertices:

$$\sum_j \left( \rho \int_{\Omega} \mathbf{N}_j \mathbf{N}_i \, dV \right) \ddot{\mathbf{x}} = \mathbf{f}_{\text{ext}} + \sum_j \left( \int_{\Omega} \mathbf{B}_j \mathbf{E} \mathbf{B}_i \, dV \right) \mathbf{u}, \quad (22)$$

for all vertices  $i$ . This holds for each continuous element  $e$ :

$$\rho V^e \mathbf{N}^{eT} \mathbf{N}^e = \mathbf{f}_{\text{ext}}^e + \mathbf{B}^{eT} \mathbf{E} \mathbf{B}^e V^e \mathbf{u} \quad (23)$$

For this article, the following Lagrangian dynamic deformation equation<sup>29</sup> is used to describe the elastic deformation of a material.

$$\mathbf{M}\ddot{\mathbf{x}} + \mathbf{D}\dot{\mathbf{x}} + \mathbf{K}(\mathbf{x} - \mathbf{x}_0) = \mathbf{f}_{\text{ext}}, \quad (24)$$

where

$$\mathbf{M}^e = \rho V^e \mathbf{N}^{eT} \mathbf{N}^e, \quad (25)$$

$$\mathbf{K}^e = \mathbf{B}^{eT} \mathbf{E} \mathbf{B}^e V^e, \quad (26)$$

are the elemental mass and stiffness matrix, respectively, derived from Equation (23) and  $\mathbf{D} = \alpha\mathbf{M} + \beta\mathbf{K}$  is the Rayleigh damping matrix.

Linear elastic forces only require the stiffness matrix  $\mathbf{K}$  to be computed once at initialization. They also work well with an implicit Euler solver used for this article. In order to avoid the drawbacks associated with linear stiffness, we use elemental-warped stiffness.<sup>30</sup> This is achieved by extracting the rotational part  $\mathbf{R} \in \mathbb{R}^{3 \times 3}$  from the tetrahedron's deformation. The deformed position  $\mathbf{x}$  can be rotated back to its unrotated position with  $\mathbf{x}_i \mathbf{R}^{-1}$ . The internal force  $\mathbf{K}(\mathbf{x} - \mathbf{x}_0)$  from Equation (24) is computed with the unrotated  $\mathbf{x}$  and then rotated back. See Müller and Gross<sup>30</sup> for a fuller description of this.

### 7.3 | Humidity interface

The dynamic deformation of the volume is controlled by changes in the object's moisture content. The removal of moisture from an object creates an imbalance between the object's internal and external pressure. This pressure imbalance creates contraction stresses that lead to the shrinkage observed in drying material. Mayor and Sereno<sup>31</sup> assume that the total mass of an object consists of dry solid, water, and air. The air contribution is generally required to compute the porosity of the material. For this article, the air contribution an object's mass has been omitted for simplicity.

Shrinkage in an object's volume is often described by the volumetric shrinkage coefficient  $S_v = \frac{V}{V_0}$ , where  $V$  and  $V_0$  are the current and initial volume of the object, respectively.<sup>14,27</sup> In order to model shrinkage, correlation between volume loss and moisture content needs to be described. Mayor and Sereno<sup>31</sup> provide an overview of different empirical and fundamental shrinkage models, most of which describe the shrinkage of vegetables. There is, however, a model for describing the volume shrinkage of a slab of beef:

$$S_v = \frac{1}{1 - \rho} \left( 1 + \frac{\rho_0(\phi - \phi_0)}{\rho_w(1 + \phi_0)} - \rho_0 \right). \quad (27)$$

Here  $\rho_0$  and  $\rho$  are the initial and current porosity of the material and  $\rho_w$  is the density of water. The porosity term is kept at 0 throughout the simulation, as we found that its effect on visual realism is negligible. With this the volume shrinkage becomes:

$$S_v = 1 + \frac{\rho_0(\phi - \phi_0)}{\rho_w(1 + \phi_0)}. \quad (28)$$

By contrast to the method by Liu et al.,<sup>14</sup> the density term  $\frac{\rho_0}{\rho_w}$  is considered for this simulation when computing the volume shrinkage coefficient.

The volume shrinkage coefficient is used to calculate the shrinkage strains that drive the object's deformation, as described by Liu et al.<sup>14</sup> and Yang et al.<sup>27</sup>

$$\boldsymbol{\varepsilon}_{ml} = \gamma [S_v^{1/3} \ S_v^{1/3} \ S_v^{1/3} \ 0 \ 0 \ 0]^T. \quad (29)$$

Let  $\mathbf{u}_{ml}$  be the deformation caused by moisture loss. Then, the internal forces due to moisture loss can be described by:

$$\begin{aligned} \mathbf{f}_{ml}^e &= \mathbf{R}^e \mathbf{K}^e \mathbf{u}_{ml} \\ &= \mathbf{R}^e \mathbf{K}^e \mathbf{B}^{e-1} \boldsymbol{\varepsilon}_{ml} \quad (\text{since } \boldsymbol{\varepsilon} = \mathbf{B}\mathbf{u}) \\ &= \mathbf{R}^e (V^e \mathbf{B}^{eT} \mathbf{E} \mathbf{B}^e) \mathbf{B}^{e-1} \boldsymbol{\varepsilon}_{ml} \\ &= \mathbf{R}^e V^e \mathbf{B}^{eT} \mathbf{E} \boldsymbol{\varepsilon}_{ml}, \end{aligned} \quad (30)$$

where  $\mathbf{R}^e$  is the tetrahedral rotation matrix from the elemental-warped stiffness by Müller et al.<sup>30</sup> The total strain is the sum of the elastic strain and the strain caused by water loss, that is,  $\boldsymbol{\varepsilon}_{total} = \boldsymbol{\varepsilon}_{elastic} + \boldsymbol{\varepsilon}_{ml}$ . Hence, the final system of second-order ordinary differential equations (ODE) to solve the volume deformation is:

$$\mathbf{M}\ddot{\mathbf{x}} + \mathbf{D}\dot{\mathbf{x}} + \mathbf{K}'\mathbf{x} + \mathbf{f}'_0 - \mathbf{f}_{ml} = \mathbf{f}_{ext}, \quad (31)$$

which considers the forces  $\mathbf{f}_{ml}$  from the changes in water content and can be solved with the same techniques as the moisture diffusion ODE.

## 8 | SKIN DEFORMATION AND SHADING

As the internal volume shrinks, the skin undergoes similar structural changes. The skin compresses due to water loss but is also pulled along the deformation of the volume mesh. This results in the skin clinging firmly to the underlying layers and wrinkling. Similar effects have been achieved when simulating fruit rotting, as described by Liu et al.<sup>14</sup> and Kider et al.,<sup>18</sup> by defining the skin mesh as a mass-spring system. However, the deformation behavior is very dependent on the spring network structure and tuning the constants in mass-spring systems can be difficult. For this article, position based dynamics<sup>2</sup> are used to solve the skin deformations, as they allow for direct control over the vertices' positions and wrinkle formation. This allows for the simulation of fine wrinkles on thin areas, such as fingers, and larger wrinkles and folds on the arm, rather than the skin buckling effects observed in fruit rotting. Furthermore, position based dynamics allow for stable simulations.

### 8.1 | Position based dynamics

Müller et al. represent the deformable object by a set of  $N$  particles and  $M$  constraints.<sup>2</sup> Each particle has mass, position, and velocity. Constraints are defined by a constraint function and have a stiffness parameter that defines their strength. The dynamic deformation of the object is simulated by estimating new particle positions due to external forces, which are then corrected to satisfy predefined constraints. Explicit Euler integration is used to compute new approximate positions. At each time step the new velocity due to external forces of each particle is computed. Damping is applied to the velocities at this point. The damped velocities are then used to compute estimated positions ( $\mathbf{p}_i$ ). With the estimated positions known, the collision can be detected and collision constraints generated. The estimated positions need to be corrected such that the  $M + M_{collision}$  constraints are satisfied. This is done iteratively using a Gauss-Seidel type solver.

In our model, the vertices of the triangle mesh representing the skin act as the particles. As for the constraints controlling the deformation, Müller et al.<sup>2</sup> provide different types of constraints. Since we aim for a cloth-like skin deformation we use stretching constraints and bending constraints. The constraints for both types are constructed at the start of the simulation. Additional collision constraints are constructed at each iteration of the solver.

Stretch constraints are constructed for each edge. An initial length (or rest length) of the connecting edge is computed during constraint initialization. At each iteration the current distance between the predicted positions of the two edge vertices is computed (predicted length). The constraint function for a stretching constraint is described by the difference of the rest length and the predicted length.<sup>2</sup> We increase the stiffness parameter of stretching constraints with water loss to achieve the stiffer dynamics as the skin turns leathery. Bending constraints are constructed for each triangle pair sharing an edge. The bending is described by changes in the angle  $\theta$ , which lies between the face normals of the two triangles.<sup>2</sup> Computing the correction vector for each vertex involves finding the derivatives of the constraint functions with respect to the two points (for stretching and collision) and four points (for bending).

We have now defined the set of skin constraints that drive the internal forces of the surface mesh. In order to drive the deformation, we need to find the new velocity due to external forces, such as gravity and pulling forces caused by the volume deformation. This will be described in the following section.

## 8.2 | Connection of skin to volume

In a living body the epidermis is attached to the underlying dermis by the basement membrane.<sup>32</sup> As the internal parts of the body (subcutaneous tissue and muscle tissue) shrink due to dehydration so does the skin. The attachment of the two layers is modeled by connecting every vertex of the skin mesh to the underlying volume mesh using tracking points. These are located on the internal volume's boundary faces. A vertex's tracking point is the point at which a vector along the negative normal direction of the vertex intersects the volume boundary. The tracking point is described by the three vertices of the triangle face it intersects, using barycentric coordinates. This means that, as the internal volume mesh deforms, the tracking points located on its boundary move along. In addition, the initial distance between the vertex and tracking point is stored for each connection. The new positions of the tracking points and the initial distances can then be used to compute the new positions of the skin vertices using the Müller et al. position based dynamics described above. See Figure 1 for a diagram of a tracking connection between the surface mesh and the volume mesh.

Müller and Chentanez propose an improvement to position based dynamics that is capable of adding more wrinkles to the cloth or skin animations using attachment constraints.<sup>33</sup> A similar technique is used here to drive the skin vertex displacement caused by the deformation of the internal volume. The tracking connections are used to construct tracking constraints, based on Müller's and Chentanez's<sup>33</sup> attachment constraints.

Figure 2 shows a diagram describing a tracking (or attachment) constraint. The vertex with position  $\mathbf{p}_i$  is connected to the tracking point  $\mathbf{t}_i$ . An initial radius  $r_j$  controls the maximum distance that  $\mathbf{i}_i$  is allowed to move away from  $\mathbf{t}_i$ . The correction vector  $\Delta\mathbf{p}_i$  is only calculated and applied if  $|\mathbf{t}_i - \mathbf{p}_i| > r_j$ . Attachment and tracking constraints are similar to stretch constraints, but with only the vertices on the triangle mesh being allowed to move, resulting in the following constraint function:

$$C_{\text{tracking}}(\mathbf{p}_i, \mathbf{t}_i) = |\mathbf{t}_i - \mathbf{p}_i| - r_j. \quad (32)$$

The radius  $r_j$  controls the wrinkling strength and formation. In order to induce the wrinkle effects in the Müller and Chentanez method,<sup>33</sup> this radius for attachment constraints needs to be painted on the surface mesh. In the method proposed here, a maximum radius for each tracking constraint was chosen for the entire skin surface mesh and will change in proportion to moisture loss. The radius controls the maximum distance that the skin layer is allowed to separate from the underlying volume mesh. Initially, the length of the tracking constraints will be close to zero, but will increase as the volume shrinks.

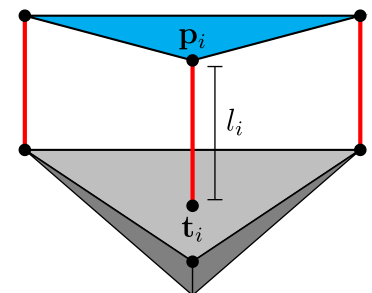


**FIGURE 1** The gray triangle face is a boundary face of the tetrahedral volume mesh. The blue triangle is a surface element from the skin mesh. Every vertex  $\mathbf{p}_i$  on the skin mesh has a tracking point  $\mathbf{t}_i$  on the boundary faces of the underlying volume mesh. The red lines are springs of length  $l_i$ , connecting each vertex to its tracking point

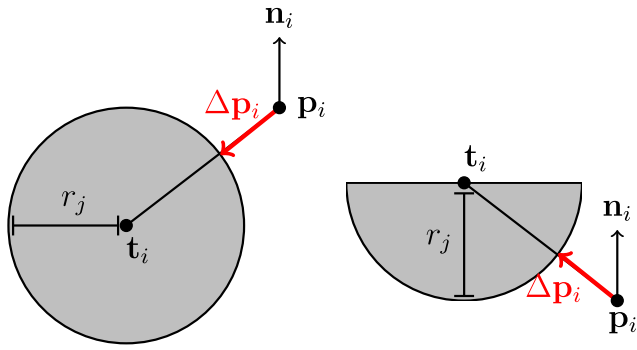


**FIGURE 2** Left: A tracking constraint (or attachment constraints<sup>33</sup>)  $j$  of a node  $i$  with position  $\mathbf{p}_i$  and tracking point  $\mathbf{t}_i$  on the volume mesh boundary. A radius  $r_j$  is assigned to the constraint, which acts as the maximum distance  $\mathbf{p}_i$  can move away from  $\mathbf{t}_i$ .  $\mathbf{n}_i$  is the vertex normal of vertex  $\mathbf{p}_i$ . Right: one sided attachment constraint<sup>33</sup> to avoid collision of the surface vertex  $\mathbf{p}_i$  with the volume boundary

Our tracking constraints differ from attachment constraints in the following respect; tracking constraints are divided into two cases, the surface constraint is pointing outward (i.e., along the vertex normal direction) or inward (along reverse normal direction), assuming a directional constraint pointing from the surface vertex toward the tracking point on the volume boundary, as shown in Figure 2. We handle the two cases separately.

An outward facing tracking constraint indicates that the vertex has penetrated the boundary of the volume mesh. In this case, the tracking constraint is treated as a one sided attachment constraint, as in Müller and Chentanez method.<sup>33</sup> For one sided attachment constraints, the stiffness is set to 1 and the radius  $r_j$  is kept constant throughout the simulation.

Using a uniform radius approach in combination with a tracking constraint resulted in smooth skin deformation with very little wrinkling formation. Therefore, we chose a different approach for inward facing constraints. Inward facing constraints are used to compute a pulling force in the direction of the tracking constraint. The strength of the force is controlled by the stiffness parameters and is only triggered if the constraint's length exceeds the radius. Let  $r_{\max}$  be the maximum radius a vertex is allowed to move away from the volume boundary, then the radius  $r_j$  for tracking constraint  $j$  is computed as follows:

$$r_j = (1 - k_j)r_{\max}, \quad (33)$$

where  $k_j$  is the constraint's stiffness.

The stiffness parameter is affected by moisture changes during the desiccation simulation. At the start, when the skin is still fully moisturized, the stiffness is large, causing the radius to be small. With the loss of moisture the radius gets larger, allowing the skin to separate more and more from the boundary of the volume mesh. The pulling force  $\mathbf{f}_{\text{pull},j}$  corresponding to tracking constraint  $j$  is computed as follows;

$$\mathbf{f}_{\text{pull},j} = \begin{cases} \nabla \mathbf{p}_i & \text{if } |\mathbf{t}_i - \mathbf{p}_i| > r_j \\ \mathbf{0} & \text{otherwise,} \end{cases} \quad (34)$$

where  $\nabla \mathbf{p}_i$  is the correction vector. The pulling force is added to the velocity after the external forces but before the damping. The subsequent damping step is important when using the pulling force as it directly affects the wrinkling formation. A low damping coefficient results in strong wrinkles, but can cause a wave like movement of the skin layer if set too small. A higher damping value removes this effect, but at the same times reduces the strength of the wrinkles. Using this method allows for greater control over the strength of wrinkling effects. In addition, it grants an easy way to simulate the separation of the epidermis from the dermis associated with mummification by desiccation (as described by Papageorgopoulou et al.<sup>25</sup>) by loosening the tracking constraints, called skin slippage.

To model the skin slippage the tracking constraints are further modified. The effects of water loss on the connection of the epidermis and dermis layers are simulated by loosening the tracking constraints to simulate skin slippage. When the moisture content on a surface node reaches a predefined threshold, the stiffness of its tracking constraint is reduced in accordance with the water loss, until it reaches zero. This will cause the skin dynamics to no longer be affected by the volume mesh, but, instead, they are driven entirely by external forces such as gravity and the internal forces of the surface mesh (stretching, bending and collision constraints). The stiffness  $k_j$  of tracking constraint  $j$  is computed as follows.

$$k_j = \begin{cases} \frac{m_i k_t}{\tau_d} & \text{if } m_i \leq \tau_d \\ 0 & \text{if } m_i < \tau_n \\ k_t & \text{otherwise,} \end{cases} \quad (35)$$

where,  $m_i$  is the moisture content of surface node  $i$ ,  $k_i$  is the initial tracking stiffness, and  $\tau_d$  and  $\tau_n$  are the moisture content thresholds from which to decrease and nullify the stiffness value, respectively. The stiffness parameters are updated before the skin deformation loop.

### 8.3 | Skin shading

Our objective is visually believable skin coloration changes rather than a chemically accurate approach. Our ad hoc skin shading approach is an extension of the method proposed by Frerichs et al.<sup>15</sup> used to render the skin coloration changed caused by livor mortis. This work represents the skin as two layers; the epidermis (top) and dermis layer (bottom), similar to the Donner et al. method,<sup>34</sup> and each layer is rendered separately. In order to get the final skin render, Frerichs et al. apply a screen space diffuse approximation approach for subsurface scattering<sup>35,36</sup> on each layer individually. The epidermis and dermis maps are then convolved into the final skin map:

$$\mathbf{c} = \omega_1 \mathbf{L}_e + (1 - \mathbf{A}_e) \circ (\omega_2 \mathbf{L}_e + \omega_3 \mathbf{L}_d), \quad (36)$$

where  $\mathbf{L}_e$  and  $\mathbf{L}_d$  are the reflections of the epidermis and dermis, respectively,  $\mathbf{A}_e$  is the absorption by melanin, and  $\omega_i$  are the weights for the convolution.

The epidermis reflectance map specifies the skin color without hemoglobin contribution over the object's surface. The melanin distribution map specifies the amount of the chromophore melanin in the body's epidermis layer. This is used to compute the light absorption by melanin when computing the hemoglobin contribution to the skin coloration inspired by Donner et al.<sup>34</sup> Coloration changes within the dermis were simulated using a look up texture based on hemoglobin  $h(x, y)$  and oxygen  $o(x, y)$  content information for each pixel  $(x, y)$ .<sup>15</sup>

In order to use this method to render skin coloration changes caused by mummification, the dermis color look-up texture, absorption by melanin and convolution weights need to be adjusted in order to account for the affects of moisture loss in the skin. We modified the look-up texture approach from Frerichs et al.,<sup>15</sup> to include coloration changes caused by humidity diffusion and hemoglobin degradation.

The u-coordinate is the hemoglobin saturation, given as:

$$s(x, y) = h(x, y) \cdot M(u(x, y), v(x, y)), \quad (37)$$

where  $M(u, v)$  is the available capacity ratio obtained from a texture map used to adjust hemoglobin concentration.<sup>15</sup> Note that with water loss the hemoglobin concentration in the dermis layer would increase. We accounted for this by slightly increasing the hemoglobin saturation with moisture loss.

Similar to the fixation of hypostasis after death,<sup>15</sup> bruising is caused by spilling of blood into surrounding tissue. Hemoglobin degradation refers to the breakdown of hemoglobin molecules which cause the coloration changes of bruises from red/blue to yellow/green.<sup>37,38</sup> The altered look up texture takes this hemoglobin degradation into account by expressing the v-coordinate as the hemoglobin degradation level ( $d$ ). The hemoglobin degradation level is a combination of the oxygen  $o(x, y)$  and humidity  $m(x, y)$  levels and is computed as follows:

$$d(x, y) = \frac{1}{2} (o(x, y) + m(x, y)). \quad (38)$$

The blood color look-up texture used for all results generated in this article is shown in Figure 3. The changes in dermis coloration are caused by the higher absorption of light due to water loss, modeled here by the orange-brown discoloration. The dermis color look up texture has been constructed to recreate the desired coloration during mummification. The method proposed to compute the hemoglobin degradation for mummification discoloration is, it should be noted, not physically or chemically correct. Instead, thinking of the hemoglobin degradation as the v-coordinate in the look up texture serves as guidance for controlling the coloration.

The absorption by melanin  $\mathbf{A}_e$  for mummification is controlled by the melanin map. The melanin map for mummification uses two color channels to specify the absorption strength for the fully hydrated and dehydrated stage. The absorption values  $\mathbf{A}_e$  are then computed with respect to the moisture content by linearly interpolating between the hydrated and dehydrated values.

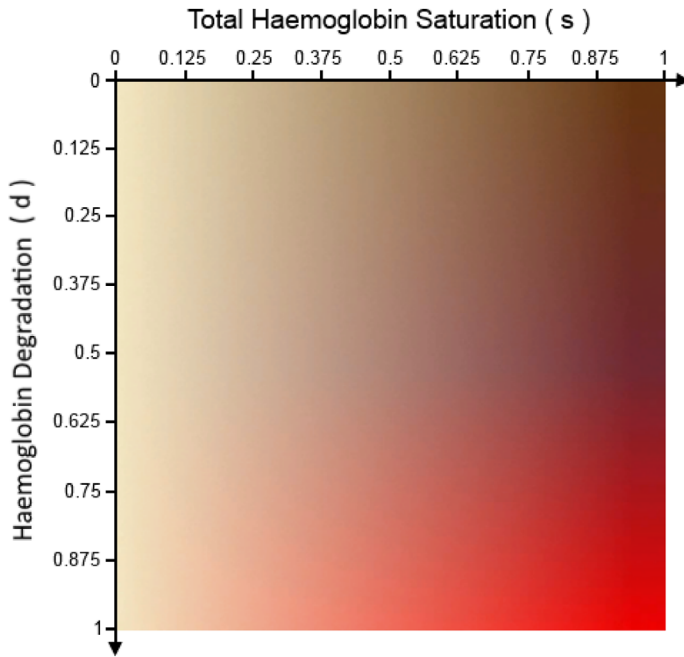


**FIGURE 3** Dermis color lookup texture used in the dermis rendering step. The total hemoglobin saturation is the fraction of hemoglobin in blood which is obtained using Equation (37). The hemoglobin degradation of the blood is obtained using Equation (38)

The mummification skin shader requires a modification of the weights, such that they consider the state of dehydration. Let  $\mathbf{w}_i$  be the Gaussian weights for the hydrated skin from Frerichs et al.<sup>15</sup> and  $\boldsymbol{\psi}_i$  the Gaussian weights for fully dehydrated skin. The weights are then defined as:

$$\begin{aligned}\omega_1 &= m\mathbf{w}_1 + (1 - m)\boldsymbol{\psi}_1, \\ \omega_2 &= m\mathbf{w}_2 + (1 - m)\boldsymbol{\psi}_2, \\ \omega_3 &= m \sum_{i=3}^6 \mathbf{w}_i + (1 - m)\boldsymbol{\psi}_3,\end{aligned}\quad (39)$$

where  $m$  is short for  $m(x, y)$ . Equation (39) describes  $\omega_1$ ,  $\omega_2$ , and  $\omega_3$  as a linear blend between the hydrated and dehydrated Gaussian weights, controlled by the moisture content. Here, dehydrated weights  $\boldsymbol{\psi}_1 = [0.070, 0.083, 0.100]$ ,  $\boldsymbol{\psi}_2 = [0.100, 0.100, 0.100]$ , and  $\boldsymbol{\psi}_3 = [0.830, 0.817, 0.800]$  are used. The values were chosen to best recreate the skin shading associated with dehydration described by Iglesias-Guitian et al.<sup>39</sup> The lower values in  $\boldsymbol{\psi}_1$  and  $\boldsymbol{\psi}_2$ , as compared with  $\mathbf{w}_1$  and  $\mathbf{w}_2$  lead to a lesser contribution of the epidermis to the skin coloration, to account for the thinning of the epidermis due to radical dehydration, which makes it more translucent.<sup>40</sup>

## 9 | RESULTS AND DISCUSSION

Our evaluation includes comparison of our results with visual images of mummification, such as the results of the lower leg mummification experiment by Papageorgopoulou et al.<sup>25</sup> Unfortunately, we could not find similar experiments for an arm which would have allowed us a more direct comparison with our arm model. The two are nonetheless sufficiently similar for evaluation purposes, since both feature long thin digits, bony joints, and more fleshy limbs, which mummify in an analogous fashion.<sup>23</sup>

Mummification by desiccation is a complex process and mummified bodies can vary greatly in appearance. Nonetheless, some common appearance patterns can be observed in desiccated mummies. In this work, the focus is on reproducing some of the most pronounced visual mummification characteristics. These include the shrinking of the soft tissues such that the underlying bone structure can be discerned, the wrinkling and folding effects of the skin and the brownish to black coloration changes of the soft tissue. The bones are generally not affected by mummification.

The geometry information for these can be seen in Table 1. Note that the skin layer on the head model is of higher resolution than the boundary of the underlying volume mesh. A PC with an Intel Core i7 CPU running at 3.40 GHz, with

**TABLE 1** This table shows the geometry information for the two models used in terms of node and polygon counts in thousands (k)

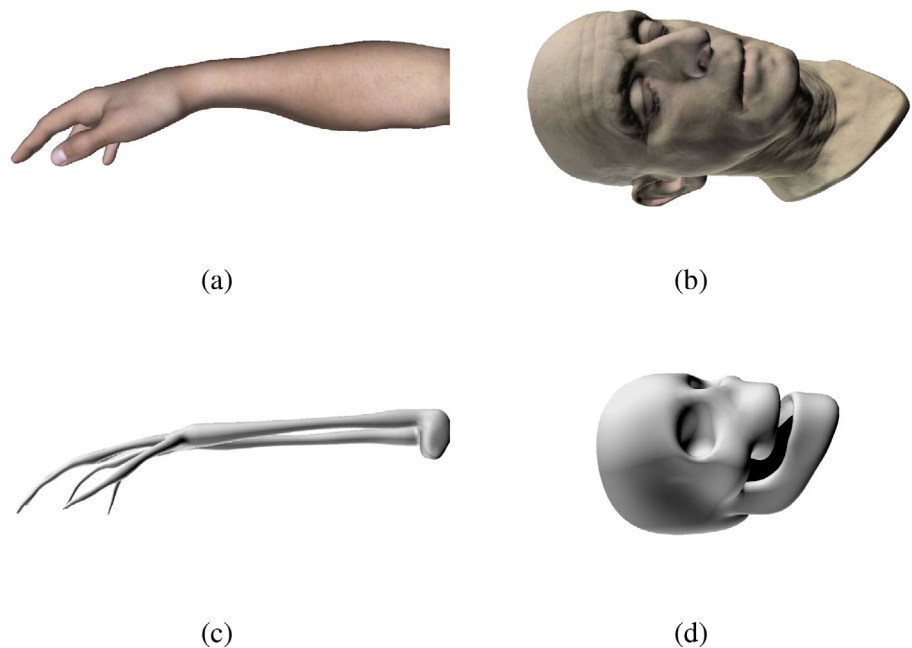
Model size	Head model (k)	Arm model (k)
Volume node count	35	29
Flesh node count	33	28
Tetrahedra count	149	141
Surface triangle count	122	19

*Note:* The volume node count is the total number of vertices of the volume mesh, whereas the flesh node count excludes the vertices of the bone mesh.

**TABLE 2** This table shows performance statistics of each of the three mummification simulation steps individually plus the time of each frame (which includes the skin rendering) in seconds (s)

Timings (in seconds)	Head model (s)	Arm model (s)
Per frame	10.930	2.933
Per dehydration step	1.463	0.372
Per volume deformation step	8.156	2.563
Per skin deformation step	1.221	0.173

**FIGURE 4** The input meshes used for the simulation. The top row shows the skin layer and the bottom row the bone layer triangle meshes. The surface mesh in (b) is a free three-dimensional model obtained from Reference 26



16 GB of RAM and a NVIDIA GeForce GTX 760 graphics card was used for the generation of the examples. Performance information is shown in Table 2. Timings are in the acceptable range for offline simulation, however, they are unsuitable for real-time simulation. For real-time use the offline results could be fitted to a set of blendshapes and associated weights, as described in Neumann et al.,<sup>41</sup> with additional vertex attributes for the humidity, hemoglobin, and oxygen contents Figure 4.

## 9.1 | Humidity diffusion

Figure 5 shows the outside (left column) and a cross section (right column) of an arm during the humidity diffusion simulation. Blue areas are saturated and red areas are deprived of all water, as described by the color scale on the right. The red line within the arm in the right column is a bone with zero moisture content. The fingers have the highest surface to flesh ratio and therefore dry out quickest, similarly to results reported by Papageorgopoulou et al.<sup>25</sup> The forearm and wrist still contain about two thirds of the initial water content. The dehydrated areas spread from the fingers and also become

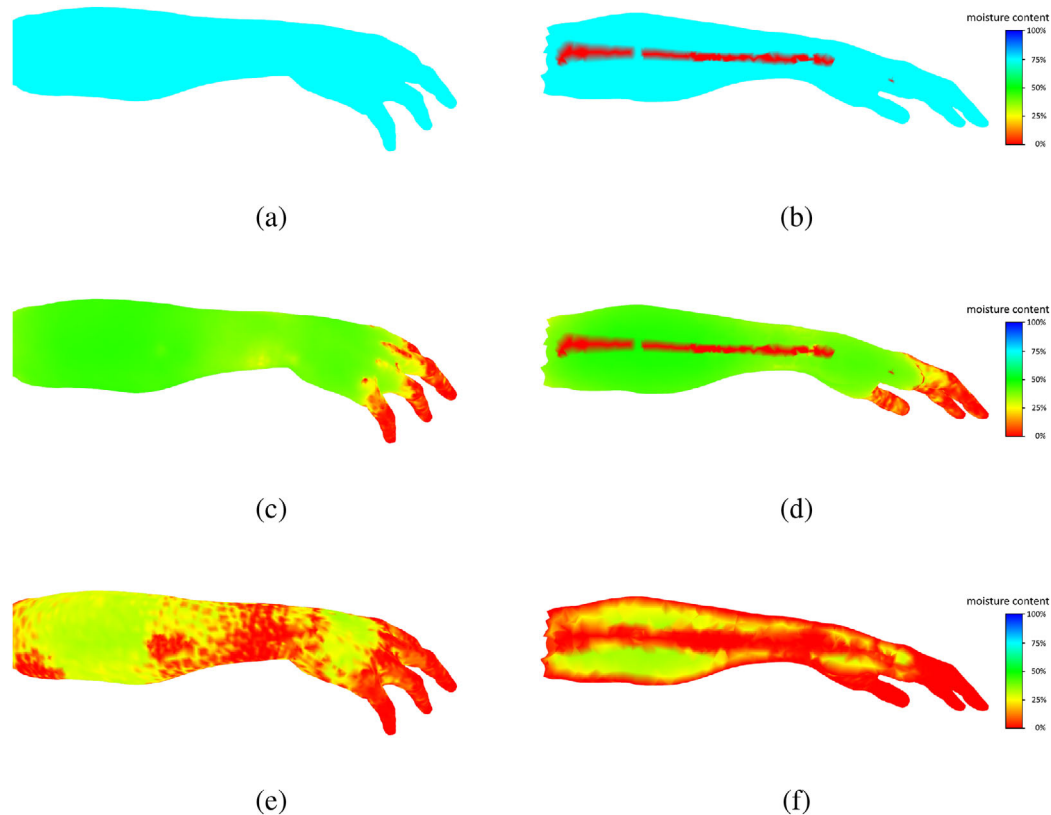


**FIGURE 5** This figure shows the results of the moisture diffusion simulation applied to the model of an arm with an internal bone structure at three different time steps. The left column shows the outside of the object, whereas the right column shows a crosscut of the arm, revealing the internal bone

more apparent at the wrist. The forearm is still mostly hydrated. Papageorgopoulou et al.<sup>25</sup> observed in their experiment that the thigh on the lower leg had not fully dehydrated by the end, due to its greater volume. This is in agreement with the result displayed in Figure 5e,f.

## 9.2 | Volume deformation

Mummification by desiccation is often accompanied by a significant volume loss. Aufderheide<sup>23</sup> and Papageorgopoulou et al.<sup>25</sup> point out the difference in mummification speed over a body. Papageorgopoulou et al.<sup>25</sup> report that the toes and foot shrunk faster than the rest of the leg. Toward the end of the experiment the soft tissue on the foot, toes, and lower leg had shrunk so much that the skin was clinging to the underlying bone structure. The thigh, however, had not fully dehydrated and therefore showed less volume loss than the lower leg. This is similar to what can be observed in Figure 6, which shows the simulation result of the arm. Note that no skin shading or skin wrinkling has been applied at this stage. Figure 6a shows the initial arm with 75% moisture content and Figure 6b shows the fully dehydrated arm. The arm has become significantly shrunken and the bone can be seen underneath the skin (see Figure 6b).

## 9.3 | Skin deformation

Two photographs of desiccated mummy parts can be seen in the top row of Figure 7. The skin of the real mummy shows noticeable wrinkling and folding over the body, especially around the neck. Finer wrinkles are noticeable on the leg. The mummification results with skin wrinkling are shown in the bottom row of Figure 7 for comparison. Figure 7c shows the simulation applied to the model of a human head. For this model, the skin mesh is of higher resolution than the underlying tetrahedral mesh. Strong wrinkles are noticeable on the neck of the model, where most of the deformation



(a)



(b)

**FIGURE 6** These images show the deformation caused by moisture diffusion on the arm model shown in (a)



(a)



(b)



(c)



(d)

**FIGURE 7** Photographs of a mummy (a) and a mummified foot (b) with skin wrinkles. The photographs were taken by the authors in the Ostkrypta in the St. Petri Cathedral in Bremen, Germany. These are compared with the simulation results on a head model (c) and arm model (d)

has taken place. This is due to the lack of underlying bone structure in the neck compared with the head (see Figure 4). The skin around the mouth and on the nose also shows some wrinkling deformations. The other areas of the head model show a more pitted skin deformation, as the loss in the underlying volume is not large enough to produce strong wrinkles. This can also be observed in the skin appearance of the head in Figure 7a. The appearance of mummified skin depends upon a number of physical and environmental factors and can vary greatly between mummies. The results of the same method applied to the arm model can be observed in Figure 7d. The arm shows smaller wrinkles, which are comparable to the wrinkling formation of the leg in Figure 7b.

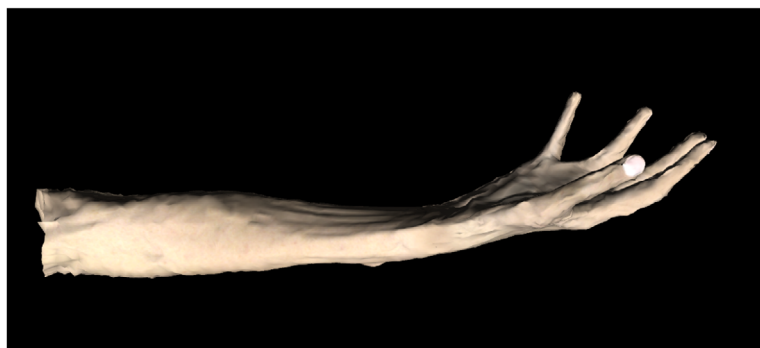
The position based dynamic approach allows for easy control of the wrinkling strength during desiccation. Figure 8 shows some simulation results on the arm model with different parameters for the skin deformation solver, shown beneath each picture. The first image (Figure 8a) shows very little wrinkling, followed by results with increased wrinkling effects. The amount of wrinkles in Figure 8b,c are comparable, however, the wrinkles in Figure 8c are larger. This can be observed around the stump and back of the arm. The photographs of mummies all show varying wrinkle strength and forms, from fine wrinkles, to buckling and big skin folds. As such, control over the wrinkling strength not only allows for more user control over the mummy's appearance, but also allows for more variety. The wrinkles' appearance depends



(a)  $r_{max} = 0.001, k_{damping} = 0.5$



(b)  $r_{max} = 0.002, k_{damping} = 0.2$



(c)  $r_{max} = 0.004, k_{damping} = 0.08$

**FIGURE 8** This figure shows mummification results with different wrinkle strengths controlled by the damping coefficient and tracking constraint radius

greatly on the triangle mesh, both in terms of where these appear and how fine they are (i.e., surface triangle count). Wrinkles form along triangles edges and are therefore dependent on the triangle layout. The size and frequency of wrinkles depend on the surface triangle count. This means that a detailed triangle mesh is required to model fine wrinkles. For very fine wrinkles a wrinkle map would be required. This would also allow for fine wrinkles to occur on the face of a triangle, as opposed to only along its edges.

## 9.4 | Skin shading

Figure 9 shows timelapse images of a mummifying arm with skin rendering. The top image shows the fully hydrated arm. The blue coloration at the bottom and pale complexion at the top represent livor mortis, produced by applying the method by Frerichs et al.<sup>15</sup> to the model before starting the mummification simulation. This was done in order to create



(a)



(b)



(c)



(d)

**FIGURE 9** This shows the skin shading results at different mummification stages. Image (a) shows the fully hydrated stages just after the fixation of hypostasis. Image (b-c) shows the partial dehydration and (d) shows full dehydration



(a)



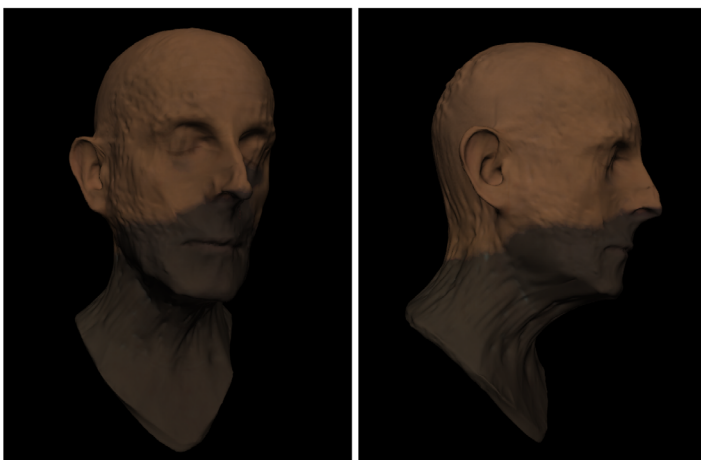
(b)

**FIGURE 10** (a) This figure shows the skin shading results due to mummification. (b) This shows a photo of a mummifying leg taken from Papageorgopoulou et al.<sup>25</sup>



(a)

(b)



(c)

(d)

**FIGURE 11** This figure shows the skin shading results at different mummification stages. Image (a) shows the skin shading just before dehydration starts. Image (b) shows the partial dehydration and (c-d) show full dehydration from different angles

a more realistic skin appearance for the mummification. In Figure 9b the arm has started to dehydrate, showing a brown coloration on the fingers that spreads to the rest of the arm in Figure 9c and, finally, covering the entire arm, as shown in Figure 9d. The areas that are full of blood have turned a darker brown than the blood deprived areas. The darker color is caused by hemoglobin degradation. The arm and back of the hand in Figure 9b appear more waxy than the skin in the top image.

The skin shading results of the mummified arm are compared with the photograph of a leg in Figure 10. The figure provides a side by side view of the leg from day 19 from Papageorgopoulou et al.<sup>25</sup> and the skin shading result of a partially mummified arm. The brownish coloration on the arm in Figure 10a is similar to the color that can be seen on the leg. Some blackened skin can also be observed in both images. However, the simulation is not able to capture the greenish coloration shown on the thigh in Figure 10b. The literature is not clear on the chemical causes of the green discoloration on the skin. A possible explanation might be hemoglobin degradation, which leads to greenish and yellow discoloration observed in healing bruises (see Bohnert et al.<sup>38</sup>). However, this greenish discoloration has not been described by the other literature discussed in the Biological Background section.

The mummification method plus skin shading was also applied to the model of the human head. The results are shown in Figure 11. Figure 11a, 11c show the changes in the skin's coloration during the mummification process. Figure 11b shows some areas dehydrated, and, as such, appearing drier and darker. Other areas, such as the neck and cheeks, are still mostly hydrated. Figure 11c,d show the skin at the fully dehydrated stage from two different angles, in which it can be observed that the dry and leathery skin is now covering the entire head.

## 10 | CONCLUSION

The main focus of this work is on recreating the visual appearance of natural mummification by desiccation for use in computer graphics-based depictions of the process and resultant outcomes in the relevant entertainment industries (computer games, VFX, and so forth). The method proposed was able to believably recreate the soft tissue shrinkage, skin wrinkling, and skin coloration effects observed in desiccated mummies. The volume representation of the internal soft tissue and bone structure allowed for the simulation of humidity diffusion within the body and the resulting contraction of the dehydrated soft tissue using the FEM. The generated humidity diffusion patterns correspond with those observed in mummification literature.

The high resolution triangle mesh representing the object's skin layer made it possible to create detailed skin wrinkling formations. The use of position based dynamics allowed for fast and controllable skin wrinkling. Although this method allows the manipulation of the strength and appearance of the wrinkles, it can cause some wave motions when watched in motion. This could be reduced, and in some cases eliminated, by damping the velocity term, but at the cost of a reduction in the strength of the wrinkling. For the skin shading an ad hoc approach was proposed, which uses a look up texture to determine the dermis coloration. The skin shader does not represent the chemical actions that cause the skin coloration changes in mummies. A more chemically accurate method would be desirable to create more realistic skin shading results. The lack of information on chemical changes in mummified skin rendered this difficult. Implementing a more accurate model to describe the light reflection properties of mummifying skin would nonetheless be an interesting subject for future research. Furthermore, as the visual material available for comparison was from light colored Caucasian individuals, our method reflected skin coloration changes on light colored skin. Further research is required to extend the method to individuals with different skin colors and ethnic backgrounds, which is another interesting area to explore with future research.

We believe the proposed method represents a valuable starting point toward creating realistic appearances of corpses for use in the digital entertainment industry as a content creation tool for artists or other parties involved in the process. Other applications for simulating human body decomposition could be in the forensic training area. This might be in the form of an interactive training tool to help the users familiarize themselves with the visual processes a body undergoes after death, and how environment variables (e.g., moisture content in the air) effect the appearance of the corpse. The physical, biological, and chemical models used to drive these appearance changes are simplified and, as such, the resulting model cannot be used for fully accurate simulations of mummification. This makes it unsuitable for any forensic or biological studies beyond the use of a training tool.

There are other factors that influence the dehydration and shrinking of the tissue, such as environmental temperature, air circulation around the body, and whether some skin is covered by cloth. These have not been considered in our approach here. Desiccation is not the exclusive cause of mummification. Instead, there is a wide variety of reasons tissue

can mummify. Even mummification by desiccation can occur under different circumstances (e.g., spontaneous and artificial) and under varying environmental conditions. Introducing these would create more realistic and varying mummies and would be another interesting future extension to our mummification method.

## ACKNOWLEDGEMENTS

We would like to thank the reviewers for constructive criticisms and suggestion that improved the article. The research presented in this article is funded by EPSRC, via the doctorate training Centre for Digital Entertainment in conjunction with Ninja Theory Ltd.

## ORCID

Dhana Frerichs  <https://orcid.org/0000-0002-1189-2193>

Andrew Vidler  <https://orcid.org/0000-0001-6342-0844>

## REFERENCES

1. Reddy JN, Gartling DK. The finite element method in heat transfer and fluid dynamics. CRC Press, 2010.
2. Müller M, Heidelberger B, Hennix M, Ratcliff J. Position based dynamics. *J Visual Commun Image Representation*. 2007;18(2):109–118.
3. Frerichs D, Vidler A, Gatzidis C. A survey on object deformation and decomposition in computer graphics. *Comput Graphics*. 2015;52:18–32.
4. Sarah F, Gibson F, Mirtich B. A survey of deformable modeling in computer graphics. Cambridge, MA: Mitsubishi Electric Research Laboratories; 1997. Technical Report TR97-19.
5. Muguercia L, Bosch C, Patow G. Fracture modeling in computer graphics. *Comput Graphics*. 2014;45:86–100.
6. Desbenoit B, Galin E, Akkouche S. Modeling cracks and fractures. *Visual Comput*. 2005;21(8-10):717–726.
7. Mérillou S, Dischler J-M, Ghazanfarpour D. Corrosion: Simulating and rendering. Paper presented at: No Description on Graphics Interface 2001, GRIN'01; Toronto, ON: Canadian Information Processing Society; 2001. p. 167–174.
8. Chang Y-X, Shih Z-C. The synthesis of rust in seawater. *Visual Comput*. 2003;19(1):50–66.
9. Dorsey J, Hanrahan P. Modeling and rendering of metallic patinas. Paper presented at: Proceedings of the 23rd Annual Conference on Computer Graphics and Interactive Techniques, SIGGRAPH '96; New York, NY: ACM; 1996. p. 387–396.
10. Dorsey J, Pedersen HK, Hanrahan P. Flow and changes in appearance. Paper presented at: Proceedings of the 23rd Annual Conference on Computer Graphics and Interactive Techniques, SIGGRAPH '96; New York, NY: ACM; 1996. p. 411–420.
11. Chen Y, Xia L, Wong T-T, Tong X, Bao H, Guo B, Shum H-Y. Visual simulation of weathering by gamma-ton tracing. Paper presented at: ACM SIGGRAPH 2005 Papers, SIGGRAPH '05; New York, NY: ACM; 2005. p. 1127–1133.
12. Günther T, Rohmer K, Grosch T. GPU-accelerated interactive material aging. Paper presented at: VMV 2012: Vision, Modeling and Visualization; 2012.
13. Jeong SH, Park S-H, Kim C-H. Simulation of morphology changes in drying leaves. *Comput Graphics Forum*. 2013;32(1):204–215.
14. Liu Y, Chen Y, Wu W, Max N, Wu E. Physically based object withering simulation. *Comput. Animat. Virtual Worlds*. 2012;23(3-4):395–406.
15. Frerichs D, Vidler A, Gatzidis C. Biologically inspired simulation of livor mortis. *Visual Comput*. 2016;1–14.
16. Boissieux L, Kiss G, Thalmann NM, Kalra P. Simulation of skin aging and wrinkles with cosmetics insight. In: Magnenat-Thalmann N, Thalmann D, Arnaldi B, editors. *Computer animation and simulation 2000. Eurographics*. Springer Vienna, 2000; p. 15–27.
17. Wu Y, Kalra P, Moccozet L, Magnenat-Thalmann N. Simulating wrinkles and skin aging. *Visual Comput*. 1999;15(4):183–198.
18. Kider JT, Raja S, Badler NI. Fruit senescence and decay simulation. *Comput Graphics Forum*. 2011;30(2):257–266.
19. Bro-Nielsen M, Cotin S. Real-time volumetric deformable models for surgery simulation using finite elements and condensation. *Comput Graphics Forum*. 1996;15:57–66.
20. Cotin S, Delingette H, Ayache N. Real-time elastic deformations of soft tissues for surgery simulation. *IEEE Trans Visualization Comput Graphics*. 1999;5(1):62–73.
21. Zhang N, Zhou X, Shen Y, Sweet R. Volumetric modeling in laser BPH therapy simulation. *Visualization Comput Graphics IEEE Trans*. 2010;16(6):1405–1412.
22. Courtecuisse H, Allard J, Kerfriden P, Bordas SPA, Cotin S, Duriez C. Real-time simulation of contact and cutting of heterogeneous soft-tissues. *Med Image Anal*. 2014;18(2):394–410.
23. Aufderheide AC. The scientific study of mummies. Cambridge: Cambridge University Press, 2003.
24. Lynnerup N. Mummies. *Am J Phys Anthropol*. 2007;134(S45):162–190.
25. Papageorgopoulou C, Shved N, Wanek J, Rühli FJ. Modeling ancient Egyptian mummification on fresh human tissue: Macroscopic and histological aspects. *Anatomical Record*. 2015;298(6):974–987.
26. TEN24-Digital-Capture. Ten24 free 3D model. <http://ten24.info/tag/free-3d-model/>, 2016. Copyright ©2016 TEN24 Media Ltd.
27. Yang H, Sakai N, Watanabe M. Drying model with non-isotropic shrinkage deformation undergoing simultaneous heat and mass transfer. *Drying Technol*. 2001;19(7):1441–1460.
28. Eisenberg MA, Malvern LE. On finite element integration in natural co-ordinates. *Int J Numer Methods Eng*. 1973;7(4):574–575.
29. Nealen A, Müller M, Keiser R, Boxerman E, Carlson M. Physically based deformable models in computer graphics. *Comput Graphics Forum*. 2006;25(4):809–836.

30. Müller M, Gross M. Interactive virtual materials. Paper presented at: Proceedings of Graphics Interface 2004, GI '04; School of Computer Science, University of Waterloo, Waterloo, ON: Canadian Human-Computer Communications Society; 2004. p. 239–246.
31. Mayor L, Sereno AM. Modelling shrinkage during convective drying of food materials: A review. *J Food Eng.* 2004;61(3):373–386.
32. Farage M, Miller K, Maibach H. Degenerative Changes in Aging Skin. Berlin, Germany: Springer; 2015;p. 1–18.
33. Müller M, Chentanez N. Wrinkle meshes. Paper presented at: Proceedings of the 2010 ACM SIGGRAPH/Eurographics Symposium on Computer Animation, SCA '10; Aire-la-Ville, Switzerland: Eurographics Association; 2010. p. 85–92.
34. Donner C, Weyrich T, d'Eon E, Ramamoorthi R, Rusinkiewicz S. A layered, heterogeneous reflectance model for acquiring and rendering human skin. Paper presented at: ACM SIGGRAPH Asia 2008 Papers, SIGGRAPH Asia '08; New York, NY: ACM; 2008. p. 140:1–140:12.
35. Jimenez J, Sundstedt V, Gutierrez D. Screen-space perceptual rendering of human skin. *ACM Trans. Appl. Percept.* 2009;6(4):23:1–23:15.
36. Jimenez J, Zsolnai K, Jarabo A, et al. Separable subsurface scattering. *Comput Graphics Forum.* 2015;34(6):188–197.
37. Vidovič L, Milanič M, Majaron B. Assessment of hemoglobin dynamics in traumatic bruises using temperature depth profiling. Paper presented at: Biophotonics—Riga 2013; International Society for Optics and Photonics; 2013; Vol. 9032. p. 903202.
38. Bohnert M, Baumgartner R, Pollak S. Spectrophotometric evaluation of the colour of intra- and subcutaneous bruises. *Int J Legal Med.* 2000;113(6):343–348.
39. Iglesias-Guitian JA, Aliaga C, Jarabo A, Gutierrez D. A biophysically-based model of the optical properties of skin aging. *Comput Graphics Forum.* 2015;34(2):45–55.
40. Querleux B. *Computational Biophysics of the Skin.* Singapore: Jenny Stanford Publishing, 2016.
41. Neumann T, Varanasi K, Wenger S, Wacker M, Magnor M, Theobalt C. Sparse localized deformation components. *ACM Trans Graphics (TOG).* 2013;32(6):179.

## SUPPORTING INFORMATION

Additional supporting information may be found online in the Supporting Information section at the end of this article.

**How to cite this article:** Frerichs D, Vidler A, Gatzidis C. Computer graphics simulation of natural mummification by desiccation. *Comput Anim Virtual Worlds.* 2020;31:e1927. <https://doi.org/10.1002/cav.1927>